JOURNAL OF VIROLOGY, Nov. 2006, p. 11055–11061 Vol. 80, No. 22
0022-538X/06/$08.00+0 doi:10.1128/JVI.00933-06

Global Structural Changes in Hepatitis B Virus Capsids Induced by the Assembly Effector HAP1▽†

Christina R. Bourne,[1] M. G. Finn,[2] and Adam Zlotnick[1]*

Department of Biochemistry and Molecular Biology, University of Oklahoma Health Sciences Center, 975 E. 10th Street, Oklahoma City, Oklahoma 73104,[1] and Department of Chemistry, The Scripps Research Institute, 10666 Torrey Pines Dr., La Jolla, California[2]

Received 8 May 2006/Accepted 23 August 2006

Hepatitis B virus (HBV) is a leading cause of liver disease and hepatocellular carcinoma; over 400 million people are chronically infected with HBV. Specific anti-HBV treatments, like most antivirals, target enzymes that are similar to host proteins. Virus capsid protein has no human homolog, making its assembly a promising but undeveloped therapeutic target. HAP1 [methyl 4-(2-chloro-4-fluorophenyl)-6-methyl-2-(pyridin-2-yl)-1,4-dihydropyrimidine-5-carboxylate], a heteroaryldihydropyrimidine, is a potent HBV capsid assembly activator and misdirector. Knowledge of the structural basis for this activity would directly benefit the development of capsid-targeting therapeutic strategies. This report details the crystal structures of icosahedral HBV capsids with and without HAP1. We show that HAP1 leads to global structural changes by movements of subunits as connected rigid bodies. The observed movements cause the fivefold vertices to protrude from the liganded capsid, the threefold vertices to open, and the quasi-sixfold vertices to flatten, explaining the effects of HAP1 on assembled capsids and on the assembly process. We have identified a likely HAP1-binding site that bridges elements of secondary structure within a capsid-bound monomer, offering explanation for assembly activation. This site also interferes with interactions between capsid proteins, leading to quaternary changes and presumably assembly misdirection. These results demonstrate the plasticity of HBV capsids and the molecular basis for a tenable antiviral strategy.

Hepatitis B virus (HBV) is a small DNA virus with an enveloped T = 4 icosahedral capsid composed of 240 copies of core protein and a minor population of T = 3 capsids composed of 180 copies of core protein. Protein subunits are found in four quasi-equivalent protein chain positions, A through D, arranged as AB and CD dimers (see Fig. 2C). Multiple points in the replication cycle of HBV (24), including reverse transcription of pregenomic RNA and cellular trafficking (35), are dependent on proper capsid formation (25).

Perturbing HBV assembly, altering either the timing or the geometry of capsid formation, is expected to interfere with viral infection (42). In cultured cells, heteroaryldihydropyrimidine (HAP) molecules, such as BAY41-4109, lead to decreased production of virions and accelerated loss of capsid protein to proteasomal digestion (8). In vitro, excess BAY41-4109 led to misdirection of assembly (11). HAP1 [methyl 4-(2-chloro-4-fluorophenyl)-6-methyl-2-(pyridin-2-yl)-1,4-dihydropyrimidine-5-carboxylate], a related small molecule, was found to accelerate capsid assembly kinetics, while stoichiometric concentrations of HAP1 misdirect assembly, yielding nonicosahedral hexagonal arrays of capsid protein (26). HAP1 also bound preformed capsids and triggered disassembly, which was exacerbated by capsid-destabilizing conditions (26).

To ascertain the structural basis for HAP1 activity, we have determined the 5.05-Å structure of a variant of the *adyw* strain HBV capsid (residues 1 to 149) complexed with HAP1 (referred to as +HAP1). To facilitate comparison, we have also determined the structure of this variant in the absence of HAP1 (−HAP1) to 3.95 Å. We find structural changes resulting from binding HAP1 that suggest a molecular basis for HAP1 activity. We also identify a putative HAP1-binding site, defining a target for assembly-directed anti-HBV molecules.

MATERIALS AND METHODS

Sample preparation. Hepatitis B virus strain *adyw*, truncated at residue 149, had three native cysteine residues (positions 47, 61, and 102) replaced by alanine and an additional cysteine added at position 150 (QuikChange Multi-Site-Directed Mutagenesis kit; Stratagene). This construct was expressed in *Escherichia coli* and purified as previously described with minor modifications (38). Briefly, after separation by using Sepharose CL4B chromatography resin (Amersham Biosciences), fractions corresponding to assembled capsids were precipitated by ammonium sulfate and further purified by velocity sedimentation through a linear 10 to 40% sucrose gradient. Clear bands were evident for both T = 3 and T = 4 capsid sizes. The T = 4 band was excised by side puncture and dialyzed for crystallization without further purification.

Crystallization. Crystallization was optimized from previously reported conditions for the *adyw* subtype (41) and primarily involved replacement of the precipitant (isopropanol) with 2,3-butanediol to ease downstream crystal handling. Cocrystals were grown with the addition of a twofold molar excess of racemic HAP1 in ethanol (relative to the dimers within the capsid) followed by at least a 1-hour incubation at room temperature prior to crystallization setup. Synthesis of HAP1 has been previously described (26), and its structure is shown in Fig. S6C in the supplemental material. Growth was carried out at room temperature with 4- to 6-μl sitting drops and was initiated by a 1:1 mixture with a well solution. The protein solution contained 10 mg/ml capsid-bound dimer in 5 mM Tris, 150 mM sodium chloride, pH 7.5, and 2 to 4% ethanol. Well solutions were typically composed of 8 to 10% polyethylene glycol 5000 monomethylether, 6 to 14% 2,3-butanediol, 100 mM sodium bicarbonate, pH 9.5, 50 to 150 mM sodium chloride, and 100 to 500 mM potassium chloride. Growth of diffraction-quality crystals was rare and, for −HAP1 crystals, typically took longer than 2

* Corresponding author. Mailing address: 975 E. 10th Street, BRC 462B, Oklahoma City, OK 73104. Phone: (405) 271-9030. Fax: (405) 271-3910. E-mail: adam-zlotnick@ouhsc.edu.

† Supplemental material for this article may be found at http://jvi.asm.org/.

▽ Published ahead of print on 30 August 2006.

TABLE 1. Data collection and refinement statistics[a]

Parameter	Value[a] for:	
	−HAP1	+HAP1
X-ray source	14-BMC	14-BMD
Space group	*C*2	*C*2
Unit cell dimensions (Å, °)		
a	558.4	528.5
b	327.1	366.5
c	562.2	540.1
β	109.1	104.8
Resolution (Å)	40–3.95 (4.02–3.95)	25–5.05 (5.14–5.05)
R_{sym}[b]	0.061 (0.482)	0.094 (0.640)
Average $I/\sigma(I)$[c]	9.8 (1.3)	10.3 (1.5)
Completeness	81.8% (64.6%)	97.2% (87.5%)
Redundancy	2.0 (1.6)	3.1 (2.4)
No. of unique reflections	666,347 (26,503)	397,950 (17,849)
60-fold NCS averaging		
R factor[d]	0.316	0.313
Correlation coefficient[e]	0.894	0.889
Torsion dynamics and positional refinement		
No. of atoms[f]	4,662	4,626
RMSD bond length (Å)	0.01	0.01
RMSD bond angle (°)	1.99	1.48
R factor[g]	0.360	0.367

[a] Parentheses denote high-resolution shell statistics.

[b] $R_{sym} = \Sigma_h \Sigma_j |\langle I_h \rangle - I_j(h)|/\Sigma_h \Sigma_j I(h)$, where $I_j(h)$ is measurement number *j* of the intensity of a reflection with indices *h*.

[c] *I*, intensity.

[d] NCS averaging *R* factor = $\Sigma h\ [|F_o(h)| - k|F_c(h)|]/\Sigma h\ |F_o(h)|$, where F_c is calculated by reverse FFT of the averaged map, scaled by factor *k*.

[e] Correlation coefficient = $\Sigma h\ \{|F_o(h)| - \langle F_o(h)\rangle\}\ \{|F_c(h)| - \langle F_c(h)\rangle\}/(\{\Sigma h|F_o(h)| - \langle F_o(h)\rangle\}^2\ \{\Sigma h|F_c(h)| - \langle F_c(h)\rangle\}^2]^{1/2}$.

[f] No. of atoms refers to the icosahedral asymmetric unit.

[g] *R* factor = $\Sigma h\ [|F_o(h)| - |F_c(h)|]/\Sigma h\ |F_o(h)|$, where F_c is calculated from coordinates.

months. Excessive crystal nucleation in the presence of HAP1 was lessened by reduction of the precipitant (butanediol) or growth at 4°C.

Collection of diffraction data. Cryo-protection was accomplished by a gradual increase in the 2,3-butanediol concentration to 17 to 20% and was successful only when uncrystallized capsid was included in the mother liquor, typically at 2 mg/ml. Crystals were flash cooled in a stream of liquid nitrogen. Crystals were screened in-house prior to data collection at the Advanced Photon Source beamlines 14-BMC (−HAP1 structure) and 14BMD (+HAP1 structure). Each data set was collected from a single cryo-cooled crystal. X-ray crystallographic statistics are given in Table 1.

Structure solution and refinement. Because the unit cells were nonisomorphous, molecular replacement was carried out for each structure. For −HAP1, the *adw*-like capsid (36) template was used as a phasing model. Molecular replacement was applied with the MolRep program (33), aided by self-rotation functions calculated with GLRF (32). Subsequent efforts to refine orientation and position did not lead to any changes in the skew matrix. Phases calculated to 8 Å were subjected to 60-fold noncrystallographic symmetry (NCS) averaging and stepwise phase extension. Phases to 8 Å for the +HAP1 structure used a partially refined −HAP1 model and were extended to 5.05 Å with NCS averaging. NCS averaging was performed at one-lattice-step intervals with AVE by using masks calculated with MAMA, both from the RAVE package (15). Resulting maps were calculated with SigmaA weighting from the CCP4 program suite (5).

Refinement was carried out with CNS (3) by using strict icosahedral NCS, isotropic B-factor correction, and bulk solvent scaling. For the 5.05-Å +HAP1 structure, the bulk solvent scaling was manipulated to give satisfactory results by specifying a protein mask of a defined radius. Initial steps utilized positional refinement in conjunction with torsion molecular dynamics, with a slow-cooling schedule from 2,000 K in 50-K steps. Further positional refinement was iterated with 60-fold NCS averaging and manual rebuilding in O (12). The geometry weighting factor (w_a) was explicitly given in each run to favor geometric restraints due to the low resolution. B factors were assigned as "grouped" and used limits of 20 Å^2 to 200 Å^2 for the −HAP1 structure, with an average of 106 Å^2; the B-factor range was limited to 20 Å^2 to 300 Å^2 for the +HAP1 structure, with an average of 132 Å^2. While a test set of 5,000 reflections was flagged in thin shells and used for cross-validation, the resulting R_{free} was essentially unchanged from the crystallographic *R* factor due to NCS correlation with the refined data. Final cycles of 60-fold NCS averaging produced averaging *R* factors of 31.6% for the −HAP1 structure to a 3.95-Å resolution and 31.3% for the +HAP1 structure to 5.05 Å, with corresponding correlation coefficients of 89.4% and 88.9%, respectively. The molecular model was refined to yield crystallographic *R* factors of 36.0% for −HAP1 and 36.7% for +HAP1 structures (Table 1). These values are consistent with those for other structures solved at comparable resolutions. For example, L-A virus was solved at 3.4 Å with an averaging *R* factor of 31.0% (22), Physalis mottle virus was solved to 3.8 Å with a crystallographic *R* factor of 32.6% (17), and adeno-associated virus 2 was solved to 3 Å with a crystallographic *R* factor of 33.8% (37).

Maps were calculated using F_{obs} scaled by the negative of the Wilson B factor for each data set (B sharpened). For the $F_{obs} - F_{calc}$ map, F_{calc} contained bulk solvent scaling, and one cycle of 60-fold NCS averaging was applied to the resulting map. Superposition of maps was performed with MAVE from the RAVE package (15). Superpositions of models were carried out with O, LSQKAB (13), and LSQMAN (14) and used the α-carbons of residues 1 to 144. Capsid global superposition used fiducial markers around the symmetry axes (α-carbon of Tyr132). Buried-surface area was calculated with Areaimol (18) from the CCP4 package. Figures were generated by screen capture from O (12), rendered with Molscript (16) or Bobscript (9, 21), or from PyMol (7).

Protein structure accession numbers. The atomic coordinates and structure factors have been deposited in the RCSB Protein Data Bank (www.rcsb.org/pdb) with accession numbers 2G33 (−HAP1) and 2G34 (+HAP1).

RESULTS

Structure of *adyw* capsids. The *adyw* capsid protein differs from the protein used in a previously determined HBV capsid structure (Protein Data Bank code 1QGT) (36) at seven residues; in addition, three native cysteines were replaced with alanine. Despite the removal of Cys61, seen in an intradimer disulfide in 1QGT, the −HAP1 backbone was nearly identical, including the regions near the mutated positions (<1.6-Å root mean square deviation [RMSD]) (Table S5 in the supplemental material). There was some extension of interpretable density at the C termini compared to what was presented for 1QGT. To minimize HAP1-mediated capsid disassembly and achieve higher resolution diffraction, it was necessary to incorporate a C-terminal cysteine as residue 150, which stabilized capsids by formation of interdimer cross-links (39). No density was observed for the C-terminal residues, and no interdimer cross-links were assigned. However, without cross-links, the +HAP1 structure diffracted to only 7.7 Å (data not shown).

HAP1-mediated changes were visible in the primary data. Cocrystallization of capsids with HAP1 changed crystallization properties, crystallographic packing of particles, and unit cell dimensions, consistent over multiple crystals (Table 1; also Fig. S5 in the supplemental material). Structural changes due to HAP1 binding were readily apparent in overlays of the averaged density maps (Fig. 1). Densities corresponding to CD dimers revealed a mismatch between −HAP1 (Fig. 1, cyan) and +HAP1 (Fig. 1, magenta), evident around the quasi-sixfold vertices. This variation appeared to be on the plane of the capsid surface; the CD dimers did not appear to move radially. In contrast, the external capsid surface at the fivefold vertex, formed by AB dimers, was dominated by the +HAP1 density, which obscured the −HAP1 density. Inspection of the density

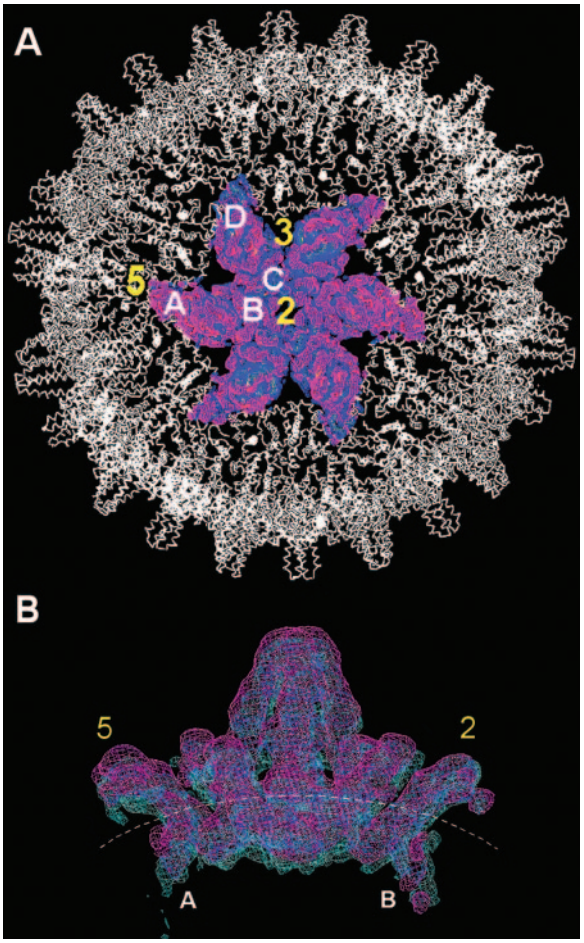

FIG. 1. Structural effects of HAP1 are visible in the electron densities of the capsid structures. The +HAP1 density is shown as a magenta mesh, the −HAP1 density as a cyan mesh. Both are contoured at 1σ. Chain identities are indicated, as are the icosahedral fivefold, twofold, and threefold vertices. (A) Density superposed at a quasi-sixfold (icosahedral twofold) vertex reveals striations indicating movement of the CD dimers largely on the plane of the capsid surface. (B) "Side" view of the AB dimer, with the capsid surface indicated by a dashed white line, highlights the hinge at the B subunit and the upward radial movement of the A subunit.

for an AB dimer from the "side" (Fig. 1B) revealed an elevation of the +HAP1 AB dimer density (magenta) relative to that of the −HAP1 dimer (cyan), with a minimum change at the outer portion of the B chain and a maximum at the outer portion of the A chain.

HAP1 affects quaternary but not tertiary structure. Molecular models were fit into averaged density maps, and structural units were superimposed to assess HAP1-mediated changes. The RMS deviations for the α-carbons of quasi-equivalent subunits were 1.0 to 1.7 Å for −HAP1 and +HAP1 structures, individually (Table S4 in the supplemental material). Comparison of monomers between the structures yielded a similar range (Table S5 in the supplemental material). This indicates that binding of HAP1 did not affect the structure of the four quasi-equivalent monomers of the capsid. Variation between monomers was localized to the top of the helix-turn-helix that forms spikes on the surface of the capsid. The flexibility of this region of the capsid was suggested by maximum B factors assigned to this loop, also seen in a previously reported crystal structure (36) (this flexibility may be related to absence of an envelope and surface proteins). Superpositions between the −HAP1 and +HAP1 models were carried out with progressively larger structural units (Table 2). Individual dimers produced RMS deviations (for α-carbons) that are within the range of quasi-equivalence. The superposition of an icosahedral asymmetric unit (α-carbons of an AB + CD dimer) from each structure yielded an RMS deviation of 1 Å and no striking changes.

HAP1 led to a global structural rearrangement of the capsid consistent with observed changes in averaged density. This change was achieved by moving each AB + CD dimer (an icosahedral asymmetric unit) as a rigid component (Fig. 2; see also Fig. 4). HAP1 induced a pivoting of the AB dimer upward out of the capsid surface, hinging near residue 132 (Fig. 2C) of chain B and leading to a radial displacement of 3.4 Å at the α-carbon of chain A residue 132 (surrounding the opening at the fivefold vertices). This movement of the A chain resulted in a protrusion of the fivefold vertices from the surface of the capsid compared to what was found for the −HAP1 structure (Fig. 2A and B). The concerted movement of the icosahedral asymmetric unit lowered the radius of the D chain by ~2 to 2.4 Å while the C chain rose ~1.6 to 2 Å, pivoting near the center of the CD dimer to maintain the same overall radial position. The displacements of the C and D subunits resulted in a flattening of the quasi-sixfold vertices (Fig. 2C). The CD dimer also rotated on the plane of the capsid surface, around a vector through the longest dimer axis (the C-terminal helix-loop-coil of the C and D chains) (Fig. 2), which resulted in a larger opening at the threefold vertices. Because the models are refined independently, the similarity of the monomers and their movements as nearly rigid bodies make it possible to reliably identify structural differences, even at 5.05-Å resolution.

Locating the HAP1-binding site. We identified a likely HAP1-binding site based on an additional electron density of approximately the right size associated with only the B and C chains of the +HAP1 structure. Analogous densities were

TABLE 2. Superpositions of −HAP1 and +HAP1 structures reveal little variation until a global fit is carried out, indicating rigid movements of (AB + CD) dimers caused by HAP1 (for α-carbon residues 1 to 144)

Unit superposed	Chain	RMSD (Å)	Observed movement(s)
AB dimer	A	1.1	None
	B	0.9	
CD dimer	C	1.0	Slight twist of D chain
	D	1.2	
AB + CD dimer	A	1.2	None
	B	0.9	
	C	1.2	
	D	1.3	
Capsid	A	2.9	AB dimer radial shift
	B	2.4	
	C	2.1	CD dimer radial and lateral shift
	D	2.0	

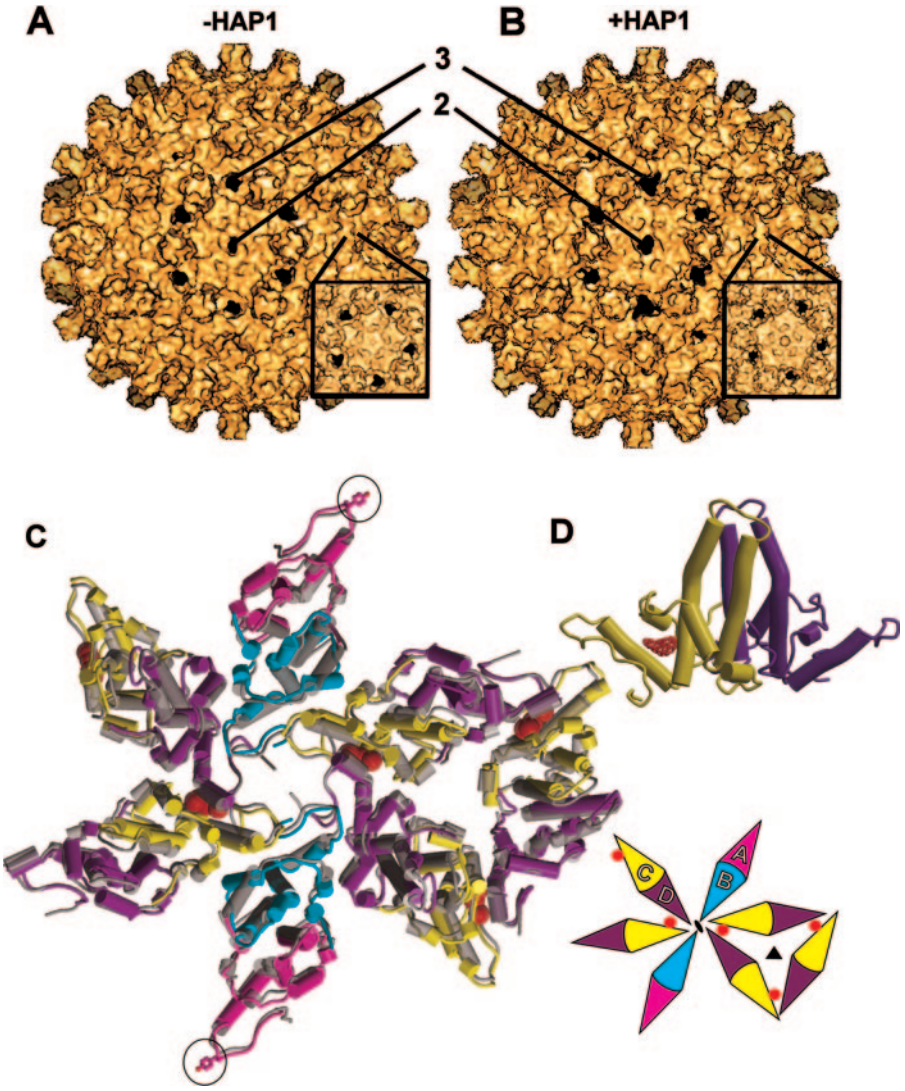

FIG. 2. HAP1 causes global structural changes. A surface rendering of the −HAP1 structure (A) and the +HAP1 structure (B), viewed looking down an icosahedral twofold (quasi-sixfold) axis; inset shows a fivefold vertex. Twofold and threefold symmetry axes are indicated. Note the changes in the shapes of the openings at all symmetry axes in +HAP1. A solvent radius of 3 Å was used in the calculation to produce a smoother surface. (C) A superposition of dimers from the −HAP1 (gray) and +HAP1 (colored) capsid structures. Magenta, chain A; blue, chain B; yellow, chain C; purple, chain D. Red spheres indicate the putative binding site of HAP1 on chain C. Note how the +HAP1 structures are pushed apart at this site. Residue Tyr132 is denoted for the A chains by a stick model; all other chains have Tyr132 in a quasi-equivalent position. A schematic of dimer arrangements surrounding the quasi-sixfold and threefold vertices is inset. The threefold and twofold (quasi-sixfold) symmetry operators are identified. (D) A CD dimer showing the putative HAP1 density from the averaged $F_{obs} - F_{calc}$ density in red (15σ). The schematic is rotated 90° on the plane of the page relative to that in panel C, and the color coding is the same.

identified at the same locations in an HBV capsid structure complexed with a brominated version of HAP1 (data not shown). This feature is strongest for the C chain (Fig. 3B), where it is as strong as the protein density in B-sharpened maps, and it is the strongest block of density (15σ) in $F_{obs} - F_{calc}$ difference maps. While the B chain also exhibits this excess density in the presence of HAP1, it is much weaker (Fig. S6 in the supplemental material), suggesting partial occupancy or disorder. The observed one HAP per dimer correlates with the crystallization conditions, which contained one HAP1 molecule (active enantiomer) per dimer. Neither the A nor the D chain has any evidence of density at this site, nor do any of the chains from the higher-resolution −HAP1 structure (Fig. S6 and S7 in the supplemental material).

The location of the putative HAP1 density is consistent with its role as an activator of assembly. Though the structure of the free dimer is not known, evidence suggests that there is a conformational change associated with assembly activation (4, 26, 27). Within a monomer, the putative HAP1 site is lined with hydrophobic residues, including Trp102, Phe23, Pro25, and Leu140. Bridging these regions of a monomer together, essentially functioning as hydrophobic glue, would stabilize the structure observed in the capsid. HAP1 localized to this hydrophobic cavity within a monomer also places it within and

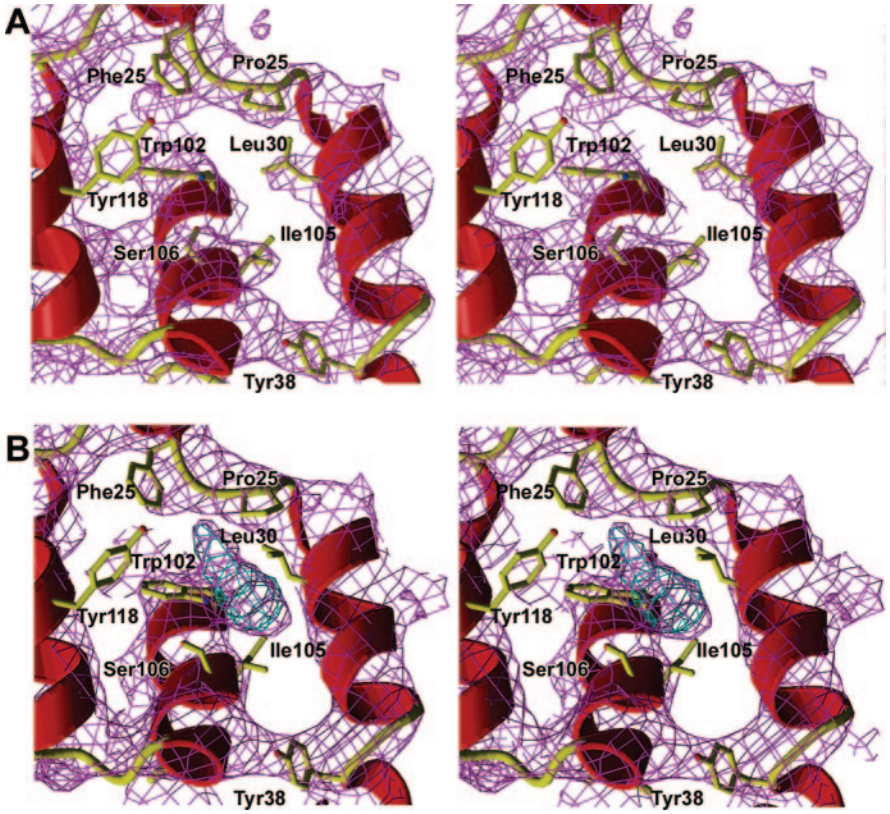

FIG. 3. The putative HAP1-binding site is located in a hydrophobic pocket that appears central to major global movements. Only the pocket of the C subunit appears to have high occupancy (for other chains, see Fig. S6 and S7 in the supplemental material); wall-eyed stereo pairs for the −HAP1 C chain (A) and +HAP1 C chain (B) are shown, with the final averaged B-sharpened electron density map contoured at 2σ (magenta); averaged $F_{obs} - F_{calc}$ density is also shown, contoured at 15σ in cyan. Ribbons indicate secondary structure; selected residues surrounding the pocket are labeled and represented as sticks. The view is roughly perpendicular to that shown in Fig. 2C.

partially obstructs a groove used to interact with a neighboring dimer, consistent with the changes in quaternary structure and the function of HAP1 as an assembly misdirector at high concentrations (26).

HAP1 binding caused a loss of ~10% of the buried surface between A chains at the fivefold vertices due to propagated movement of the AB dimer (Table 3). The capsid interface between the C and D chains (interdimer), found at the quasi-sixfold and threefold vertices, lost nearly 25% of its buried surface in the presence of HAP1 (Table 3). Neither the BC nor the BD capsid interface showed significant change in buried-surface area. The loss of buried surface occurred only at the boundaries of the icosahedral asymmetric unit. Inclusion of HAP1 in the extra density at the CD (interdimer) interface would provide a compensatory gain in buried surface to offset the observed loss (Fig. 4). The changes in buried-surface area and the positions of the putative binding sites at the threefold and quasi-sixfold vertices are consistent with the excess of hexamers in the assembly products of HAP1-misdirected reactions (26).

TABLE 3. The buried-surface area is changed by HAP1, affecting the global capsid structure

Capsid interface	Value for:		
	−HAP1 (Å^2)	+HAP1 (Å^2)	ΔHAP1 (Å^2)
AA	1589	1451	-138
BC	1274	1268	-6
BD	1501	1481	-20
CD	1389	1054	-335

DISCUSSION

The putative location of the HAP1-binding site is appealing because it correlates with structural changes and explains HAP1 activity. There are strong arguments for the authenticity of this assignment. (i) This density, observed only in the +HAP1 structure, is as strong as the protein backbone in a $2(F_{obs}) - F_{calc}$ map (>4σ) and is greater than 15σ in an $F_{obs} - F_{calc}$ map. (ii) The size and shape of this density (Fig. 3; also Fig. S6 in the supplemental material) are not planar but exhibit a slight curvature consistent with the structure of HAP1. (iii) The putative binding pocket is hydrophobic and complementary in shape to HAP1. (iv) The density is localized to areas with the largest structural changes, correlating with both movements and the loss of buried surface. Previously, another HAP molecule was successfully cross-linked to a histidine residue (8); we note that His51 and His104 are close, though not adjacent, to the putative HAP1-binding site.

Given this location, we can develop a rationale for HAP1

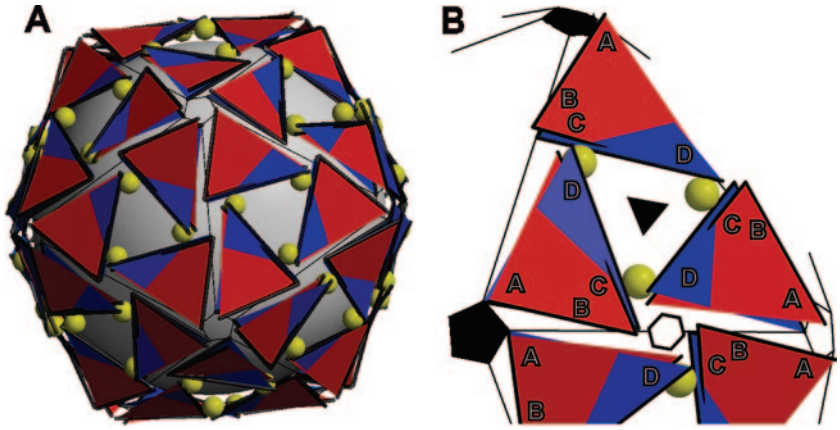

FIG. 4. A schematic representation of the global structural changes induced by HAP1. (A) A schematic of a capsid showing the global structural movement of icosahedral asymmetric units (triangles composed of an AB + CD dimer). Blue, −HAP1; red, +HAP1. Movements have been exaggerated (approximately 3×) for clarity; a yellow sphere at each C chain indicates the putative HAP1 site; the protrusion of fivefold vertices is particularly evident. (B) A close-up of an icosahedral facet shows how HAP1 changes the relationship between the icosahedral asymmetric units; symmetry operators are identified.

activity. HAP1 favors assembly because its putative binding pocket stabilizes a capsid-bound dimer structure by associating the C terminus, which is probably very flexible in the dimer form, with the central four-helix bundle at the dimer interface. Localization of HAP1 in this density generates a triangle of dimers around the icosahedral threefold vertex, with a HAP1 at each corner (Fig. 2C). As capsid assembly is nucleated by a trimer of dimers (40) and such a triangle is also consistent with the hexagonal lattice observed in assembly induced by high HAP1 (26), we are led to speculate that HAP1 may also enhance assembly kinetics by promoting or stabilizing capsid nuclei. HAP1 destabilizes preformed capsids by, at a minimum, weakening fivefold vertices. Recent results suggest destabilization of assembled capsids at stoichiometries of one HAP1 per dimer and greater (29). HAP1 causes a flattening of quasi-sixfold vertices, which could contribute to the hexameric oligomers formed in solution when there is excess HAP1 (26). Previous observations indicate a switch from enhanced assembly at ratios of up to one HAP1 per two dimers (which could be accomplished by HAP1 binding to C chains) to misdirected assembly at higher HAP1 ratios, with a maximum effect achieved at one HAP1 per dimer (26). We have avoided the more drastic destabilizing effects of HAP1 (26) by covalent cross-linking of capsids utilizing the C-terminal cysteine. Misdirection of assembly would be expected when capsid protein is saturated with HAP1 because it favors threefold and quasi-sixfold structures.

Global HBV capsid plasticity was achieved by moving nearly rigid bodies (an AB + CD dimer) linked by icosahedral symmetry (Fig. 4), similar to what was found for other viruses known to change quaternary structure by moving protein subunits as near-rigid bodies (1, 6, 20, 30). It is interesting to note that destabilization of fivefold vertices appears to be a common feature in virus transitions (10, 19, 31). HBV capsid flexibility is proposed to transduce signals during the viral life cycle. Recent cryo-electron microscopy structures of HBV RNA- and DNA-filled capsids suggested a subtle movement within the dimer (23), while image reconstructions of HBV with inserts at the spikes showed large rotations of subunits leading to deformation of individual dimers (2). Our structure with HAP1 demonstrates that a much greater range of motion is accessible to a capsid while maintaining individual dimer structures.

Capsid proteins and the process of their assembly have no cellular analogs, making them attractive virus-specific therapeutic targets. We have identified a likely binding site for HAP1 that provides molecular rationales for allosteric activation and misdirection of HBV capsid assembly (26). Because of the capsid-destabilizing activity of HAP1, the +HAP1 structure should be considered a snapshot of a metastable step in the disassembly process, providing a trajectory for the early stages in capsid disruption. As the rules for regulating and deregulating assembly are determined for different viruses, targeting assembly holds promise for a new generation of antiviral therapeutics (42). Recent development of high-throughput methods for screening potential anti-HBV capsid-specific molecules will help identify molecules that use this and other mechanisms for affecting capsid assembly and structure (28, 34).

ACKNOWLEDGMENTS

This work was supported by grants from the American Cancer Society and NIH (RSG-99-339-04-MBC and R01-AI 067417, to A.Z.) and an American Cancer Society-Mary Horton postdoctoral fellowship (PF-05-237-01-GMC, to C.R.B.). Use of the Advanced Photon Source was supported by the U.S. Department of Energy, Basic Energy Sciences, Office of Science, under contract W31-109-Eng-38.

We thank the beamline staff at the Advanced Photon Source BioCARS beamlines. We thank Stephen Stray, Philip Bourne (OSU), Jack Johnson, Jeff Speir, and Tianwei Lin (TSRI), and Mavis Agbandje-McKenna (University of Florida) for advice and assistance.

REFERENCES

1. **Belnap, D. M., D. J. Filman, B. L. Trus, N. Cheng, F. P. Booy, J. F. Conway, S. Curry, C. N. Hiremath, S. K. Tsang, A. C. Steven, and J. M. Hogle.** 2000. Molecular tectonic model of virus structural transitions: the putative cell entry states of poliovirus. J. Virol. **74:**1342–1354.
2. **Bottcher, B., M. Vogel, M. Ploss, and M. Nassal.** 2006. High plasticity of the hepatitis B virus capsid revealed by conformational stress. J. Mol. Biol. **356:**812–822.
3. **Brunger, A. T., P. D. Adams, G. M. Clore, W. L. Delano, P. Gros, R. W. Grosse-Kunstleve, J.-S. Jiang, J. Kuszewski, N. Nilges, N. S. Pannu, R. J. Read, L. M. Rice, T. Simonson, and G. L. Warren.** 1998. Crystallography and

NMR system (CNS): a new software system for macromolecular structure determination. Acta Crystallogr. D **54:**905–921.
4. **Ceres, P., and A. Zlotnick.** 2002. Weak protein-protein interactions are sufficient to drive assembly of hepatitis B virus capsids. Biochemistry **41:** 11525–11531.
5. **Collaborative Computational Project, Number 4.** 1994. The CCP4 suite: programs for protein crystallography. Acta Crystallogr. D **50:**760–763.
6. **Conway, J. F., W. R. Wikoff, N. Cheng, R. L. Duda, R. W. Hendrix, J. E. Johnson, and A. C. Steven.** 2001. Virus maturation involving large subunit rotations and local refolding. Science **292:**744–748.
7. **Delano, W. L.** 2002. The PyMOL molecular graphics system, version 0.98. DeLano Scientific, San Carlos, Calif.
8. **Deres, K., C. H. Schroder, A. Paessens, S. Goldmann, H. J. Hacker, O. Weber, T. Kramer, U. Niewohner, U. Pleiss, J. Stoltefuss, E. Graef, D. Koletzki, R. N. Masantschek, A. Reimann, R. Jaeger, R. Gross, B. Beckermann, K. H. Schlemmer, D. Haebich, and H. Rubsamen-Waigmann.** 2003. Inhibition of hepatitis B virus replication by drug-induced depletion of nucleocapsids. Science **299:**893–896.
9. **Esnouf, R.** 1997. An extensively modified version of MolScript that includes greatly enhanced coloring capabilities. J. Mol. Graph. **15:**132–134.
10. **Gan, L., J. F. Conway, B. A. Firek, N. Cheng, R. W. Hendrix, A. C. Steven, J. E. Johnson, and R. L. Duda.** 2004. Control of crosslinking by quaternary structure changes during bacteriophage HK97 maturation. Mol. Cell **14:**559–569.
11. **Hacker, H. J., K. Deres, M. Mildenberger, and C. H. Schroder.** 2003. Antivirals interacting with hepatitis B virus core protein and core mutations may misdirect capsid assembly in a similar fashion. Biochem. Pharmacol. **66:** 2273–2279.
12. **Jones, T. A., J. Y. Zou, S. W. Cowan, and M. Kjeldgaard.** 1991. Improved methods for binding protein models in electron density maps and the location of errors in these models. Acta Crystallogr. A **47:**110–119.
13. **Kabsch, W.** 1976. A solution for the best rotation to relate two sets of vectors. Acta Crystallogr. A **32:**922–923.
14. **Kleywegt, G. J.** 1999. Experimental assessment of differences between related protein crystal structures. Acta Crystallogr. D **55:**1878–1884.
15. **Kleywegt, G. J., J. Y. Zou, M. Kjeldgaard, and T. A. Jones.** 2001. Around O, p. 353–356, 366–367, International Tables for Crystallography, vol. F. Kluwer Academic Publishers, Dordrecht, The Netherlands.
16. **Kraulis, P. J.** 1991. MolScript: a program to produce both detailed and schematic plots of protein structures. J. Appl. Crystallogr. **24:**946–950.
17. **Krishna, S. S., C. N. Hiremath, S. K. Munshi, D. Prahadeeswaran, M. Sastri, H. S. Savithri, and M. R. Murthy.** 1999. Three-dimensional structure of physalis mottle virus: implications for the viral assembly. J. Mol. Biol. **289:**919–934.
18. **Lee, B., and F. M. Richards.** 1971. The interpretation of protein structures: estimation of static accessibility. J. Mol. Biol. **55:**379–400.
19. **Li, Y., J. F. Conway, N. Cheng, A. C. Steven, R. W. Hendrix, and R. L. Duda.** 2005. Control of virus assembly: HK97 "Whiffleball" mutant capsids without pentons. J. Mol. Biol. **348:**167–182.
20. **McKenna, R., D. Xia, P. Willingmann, L. L. Ilag, S. Krishnaswamy, M. G. Rossmann, N. H. Olson, T. S. Baker, and N. L. Incardona.** 1992. Atomic structure of single-stranded DNA bacteriophage phi X174 and its functional implications. Nature **355:**137–143.
21. **Merritt, E. A., and D. J. Bacon.** 1997. Raster3D photorealistic molecular graphics. Methods Enzymol. **277:**505–524.
22. **Naitow, H., J. Tang, M. Canady, R. B. Wickner, and J. E. Johnson.** 2002. L-A virus at 3.4 A resolution reveals particle architecture and mRNA decapping mechanism. Nat. Struct. Biol. **9:**725–728.
23. **Roseman, A. M., J. A. Berriman, S. A. Wynne, P. J. Butler, and R. A. Crowther.** 2005. A structural model for maturation of the hepatitis B virus core. Proc. Natl. Acad. Sci. USA **102:**15821–15826.
24. **Seeger, C., and W. S. Mason.** 2000. Hepatitis B virus biology. Microbiol. Mol. Biol. Rev. **64:**51–68.
25. **Steven, A. C., J. F. Conway, N. Cheng, N. R. Watts, D. M. Belnap, A. Harris, S. J. Stahl, and P. T. Wingfield.** 2005. Structure, assembly, and antigenicity of hepatitis B virus capsid proteins. Adv. Virus Res. **64:**125–164.
26. **Stray, S. J., C. R. Bourne, S. Punna, W. G. Lewis, M. G. Finn, and A. Zlotnick.** 2005. A heteroaryldihydropyrimidine activates and can misdirect hepatitis B virus capsid assembly. Proc. Natl. Acad. Sci. USA **102:**8138–8143.
27. **Stray, S. J., P. Ceres, and A. Zlotnick.** 2004. Zinc ions trigger conformational change and oligomerization of hepatitis B virus capsid protein. Biochemistry **43:**9989–9998.
28. **Stray, S. J., J. M. Johnson, B. G. Kopek, and A. Zlotnick.** 2006. An in vitro fluorescence screen to identify antivirals that disrupt hepatitis B virus capsid assembly. Nat. Biotechnol. **24:**358–362.
29. **Stray, S. J., and A. Zlotnick.** Bay41-4109 has multiple effects on hepatitis B virus capsid assembly. J. Mol. Recognit., in press.
30. **Taylor, D. J., N. K. Krishna, M. A. Canady, A. Schneemann, and J. E. Johnson.** 2002. Large-scale, pH-dependent, quaternary structure changes in an RNA virus capsid are reversible in the absence of subunit autoproteolysis. J. Virol. **76:**9972–9980.
31. **Teschke, C. M., A. McGough, and P. A. Thuman-Commike.** 2003. Penton release from P22 heat-expanded capsids suggests importance of stabilizing penton-hexon interactions during capsid maturation. Biophys. J. **84:**2585–2592.
32. **Tong, L., and M. G. Rossmann.** 1997. Rotation function calculations with GLRF program. Methods Enzymol. **276:**594–611.
33. **Vagin, A. A., and A. Teplyakov.** 1997. MOLREP: an automated program for molecular replacement. J. Appl. Crystallogr. **30:**1022–1025.
34. **Vogel, M., M. Diez, J. Eisfeld, and M. Nassal.** 2005. In vitro assembly of mosaic hepatitis B virus capsid-like particles (CLPs): rescue into CLPs of assembly-deficient core protein fusions and FRET-suited CLPs. FEBS Lett. **579:**5211–5216.
35. **Wieland, S. F., and F. V. Chisari.** 2005. Stealth and cunning: hepatitis B and hepatitis C viruses. J. Virol. **79:**9369–9380.
36. **Wynne, S. A., R. A. Crowther, and A. G. Leslie.** 1999. The crystal structure of the human hepatitis B virus capsid. Mol. Cell **3:**771–780.
37. **Xie, Q., T. Somasundaram, S. Bhatia, W. Bu, and M. S. Chapman.** 2003. Structure determination of adeno-associated virus 2: three complete virus particles per asymmetric unit. Acta Crystallogr. D **59:**959–970.
38. **Zlotnick, A., N. Cheng, J. F. Conway, F. P. Booy, A. C. Steven, S. J. Stahl, and P. T. Wingfield.** 1996. Dimorphism of hepatitis B virus capsids is strongly influenced by the C-terminus of the capsid protein. Biochemistry **35:**7412–7421.
39. **Zlotnick, A., N. Cheng, S. J. Stahl, J. F. Conway, A. C. Steven, and P. T. Wingfield.** 1997. Localization of the C terminus of the assembly domain of hepatitis B virus capsid protein: implications for morphogenesis and organization of encapsidated RNA. Proc. Natl. Acad. Sci. USA **94:**9556–9561.
40. **Zlotnick, A., J. M. Johnson, P. W. Wingfield, S. J. Stahl, and D. Endres.** 1999. A theoretical model successfully identifies features of hepatitis B virus capsid assembly. Biochemistry **38:**14644–14652.
41. **Zlotnick, A., I. Palmer, J. D. Kaufman, S. J. Stahl, A. C. Steven, and P. T. Wingfield.** 1999. Separation and crystallization of T = 3 and T = 4 icosahedral complexes of the hepatitis B virus core protein. Acta Crystallogr. D **55:**717–720.
42. **Zlotnick, A., and S. J. Stray.** 2003. How does your virus grow? Understanding and interfering with virus assembly. Trends Biotechnol. **21:**536–542.